Cancer Nanotechnology

RESEARCH Open Access

Theranostic RGD@Fe_3O_4-Au/Gd NPs for the targeted radiotherapy and MR imaging of breast cancer

Azadeh Amraee[1,2], Zahra Alamzadeh[2], Rasoul Irajirad[2], Abolfazl Sarikhani[2], Habib Ghaznavi[3,4], Hossein Ghadiri Harvani[5], Seied Rabi Mahdavi[1], Sakine Shirvalilou[1,2*] and Samideh Khoei[2,1*]

*Correspondence:
sakine.shirvaliloo@gmail.com;
shirvalilou.s@iums.ac.ir;
khoei.s@iums.ac.ir;
skhoei@gmail.com

[1] Medical Physics Department, School of Medicine, Iran University of Medical Sciences, P.O.Box: 1449614525, Tehran, Iran
[2] Finetech in Medicine Research Center, Iran University of Medical Sciences, Tehran, Iran
[3] Pharmacology Research Center, Zahedan University of Medical Sciences, Zahedan, Iran
[4] Cellular and Molecular Research Center, Resistant Tuberculosis Institute, Zahedan University of Medical Sciences, Zahedan, Iran
[5] Department of Medical Physics and Biomedical Engineering, Tehran University of Medical Sciences, Tehran, Iran

Abstract

Background: As a radiosensitizing agent in magnetic resonance imaging (MRI), gadolinium is disadvantageous in that it confers a rather high toxicity and low longitudinal comfort time (r_1). We hypothesized that gadolinium when combined with gold-coated iron oxide nanoparticles (NPs), might deliver better radiosensitization in MRI-based cancer theranostics. After being synthesized ligand/receptor RGD@Fe_3O_4-Au/Gd nanoparticles, they were characterized via some methods, such as visible–ultraviolet spectroscopy (UV–VIS), Fourier transform infrared spectroscopy (FTIR), dynamic light scattering (DLS), and transmission electron microscope (TEM). Using relaxometry, the parameters of contrast change in T_1-weighted MRI and the rate of radiation sensitivity on cancerous (MCF-7, SK-BR-3 and MDA-MB-231 (and reference (MCF-10a) breast cell lines were investigated.

Results: The presence of ultra-small iron oxide, gold, gadolinium, and RGD peptide as components of the RGD@Fe_3O_4-Au/Gd nanocomplex was confirmed by UV–visible, FTIR, EDX and XRD tests. With a size ranging from 4.124 nm (DLS) to 15 nm (TEM), these NPs exhibited a surface charge of –45.7 mV and a magnetic saturation of 3 emu/g. The concentrations of iron, gadolinium and gold samples in the nanocomplex were 1000, 1171 and 400 parts per million (ppm), respectively. In the relaxometry test, the rates of r_2/r_1 and r_1 NPs were 1.56 and 23.5 mM^{-1} s^{-1}. The dose increase factor for targeted (RGD@Fe_3O_4-Au/Gd) and non-targeted (Fe_3O_4-Au/Gd) NPs at 6 MV and 2 Gy was 89.1 and 59.1, respectively.

Conclusion: Owing to an enhanced signal-to-noise ratio (SNR), as confirmed by the MRI of RGD receptor-expressing MDA-MB-231 cells, RGD@Fe_3O_4-Au/Gd NPs were found to confer higher radiosensitization and an overall better performance as a novel radiosensitizer for MRI-based breast cancer theranostics than Fe_3O_4-Au/Gd nanocomplex.

Keywords: Ultra-small iron oxide magnetic NPs, Positive contrast, T1-weighted MRI, Radiation therapy, Theranostics, Breast cancer

Graphical Abstract

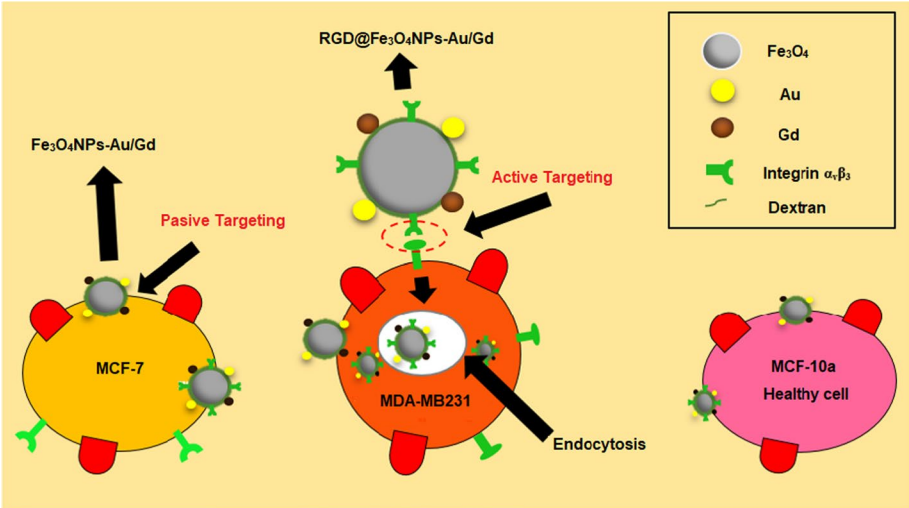

Background

Despite all recent advances in the diagnosis and treatment of breast cancer, it is still a leading cause of mortality in women throughout the world (Siegel et al. 2015). Over the last decade, there have been many improvements in the use of nanomaterials for the diagnosis and treatment of cancer, known collectively as cancer theranostics, which is the combination of therapeutic and diagnostic agents on a single platform (Yoo et al. 2011). This is because early diagnosis is of utmost importance to the overall efficiency of treatment (Lu et al. 2016), and in the case of malignancies, it is often made based on MRI findings. The contrast enhancement in MRI is much stronger than other imaging methods due to differences in proton density, and longitudinal (T1) and transverse (T2) relaxation times. Currently, most of the contrast agents used in the clinic are derived from the paramagnetic chelates of lanthanide metals such as gadolinium. Although gadolinium chelates are widely used, they are toxic compounds with a relatively low half-life in circulation and less-than-optimal traceability, which has led them to be augmented or even replaced with a host of different nanoparticles for enhancement purposes (Mendichovszky et al. 2008; Shen et al. 2017).

USPIOs (ultra-small paramagnetic iron oxide) are among these are among these contrast agents, which have recently been subject to many investigations (Ramalho et al. 2016; Shirvalilou et al. 2018). In the case of iron oxide NPs, it has been shown that as the size decreases, these NPs change from super paramagnetic into paramagnetic state. The characteristic of being superparamagnetic occurs when the nanoparticle is small enough to belong to a single domain, and decreasing the particle size tends to increase the domain size until the single domain particle (Lafta 2022). In this sense, a significant reduction in size may result in the transition of these NPs from T2 contrast agents into

their T1 counterparts (Fu et al. 2021). Positive contrast can be created by iron oxide NPs with sizes below 5 nm. The factors that differentiate these NPs from other contrast materials are their low toxicity and high signal-to-noise ratio (SNR) and super-small size with markedly low r_1 values. Thus, they can be combined with gadolinium oxide or gadolinium NPs to overcome the issues being faced with gadolinium alone. USPIOs nanocomplexes have the potential to be used as a T1-weighted MRI contrast agents (Ling et al. 2015; Zeng et al. 2015). Gold NPs (AuNPs) are one such type of nanoparticles that can be used to enhance the radiosensitizing effect of gadolinium (Ghaghada et al. 2009; Rajaee et al. 2020), since they are less likely to be trapped in the liver, excreted by the kidneys (Brissette et al. 2006) and absorbed by the endothelial cells lining the vasculature (Gaumet et al. 2008).

While the passive leakage of NPs, as a result of the enhanced permeation and retention (EPR) effect, through vessels supplying the tumors is widely used in cancer theranostics (Fang et al. 2011), it is not as reliable since NPs can become trapped within the reticuloendothelial system (Leserman et al. 1980). Conjugation of NPs with tumor-specific ligands in an effort known as active targeting is, thus, a more reliable technique (Kamaly et al. 2012), through NPs can be better concentrated at the tumor microenvironment. Several peptides expressed at the surface of tumor cells can be targeted for active delivery of NPs (Lv et al. 2012). Integrins (Hynes 2002), including αvβ3, are frequently expressed by tumor cells and exploited by targeting strategies (Schottelius et al. 2009). Peptides with RGD sequences are highly dependent on αvβ3 integrin (Pasqualini et al. 1997), hence, the incorporation of RGD peptides as coating agents into the structure of cancer-targeting nanocomplexes (Xie et al. 2008). The αvβ3 receptor is overexpressed at the levels of cancer cells such as MDA-MB-231 (Kamaly et al. 2012), while being more tightly regulated in non-cancerous breast cells like MCF-7 (Zako et al. 2009).

This study aimed to evaluate the effect of RGD@Fe_3O_4-Au/Gd nanocomplex (NP) on targeted radiotherapy and T1-weighted MRI of human breast cancer cells in vitro. Spherical RGD@Fe_3O_4-Au/Gd NPs with a size of about 15 nm were synthesized and characterized. Using relaxometry, the parameters of contrast change in T1-weighted MRI such as SNR and the amount of radiation sensitivity on cancerous (MCF-7, SK-BR-3 and MDA-MB-231 (and reference (MCF-10a) breast cell lines were investigated.

Results and discussion

Characterization of RGD@Fe_3O_4-Au/Gd

Figure 1 is a schematic illustration of RGD@Fe_3O_4-Au/Gd NPs synthesis. Physical properties of US-Fe, gadolinium-dextran-coated USPIO (Fe-Gd), Fe_3O_4-Au/Gd and RGD@Fe_3O_4-Au/Gd NPs were determined using DLS, Zeta sizer, FTIR, VSM, XRD, ICP-OES and UV/visible. The shape and size of the NPs were examined by TEM (Figs. 2 and 3). The results regarding the size and surface charge of NPs are reported in Table 1. According to the results, the optimal size for iron oxide NPs as T1 contrast agents is less than 5 nm. Based on the literature, a decrease in the size of iron oxide NPs to less than 5 nm is most likely to prompt their transition from T2 to T1 contrast medium (Chang et al. 2022; Li et al. 2022; Li et al. 2019; Wei et al. 2017).

Accordingly, we synthesized our NPs to be of a size that would correspond to this hypothesis, which we later found to hold (see Fig. 2A-C). The size of US-Fe NPs was

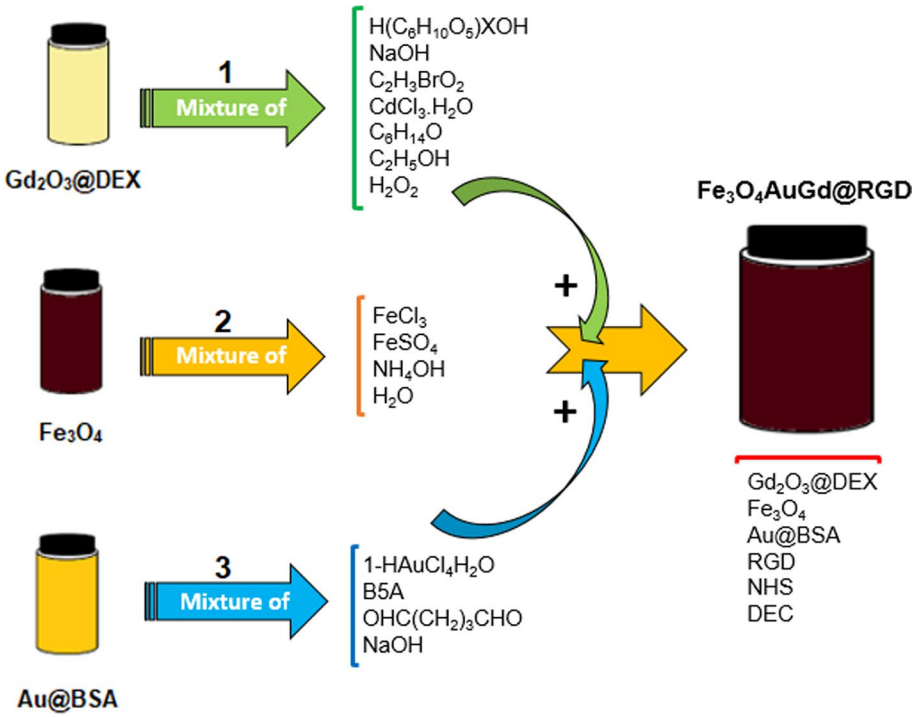

Fig. 1 The synthesis of RGD@Fe_3O_4-Au/Gd NPs

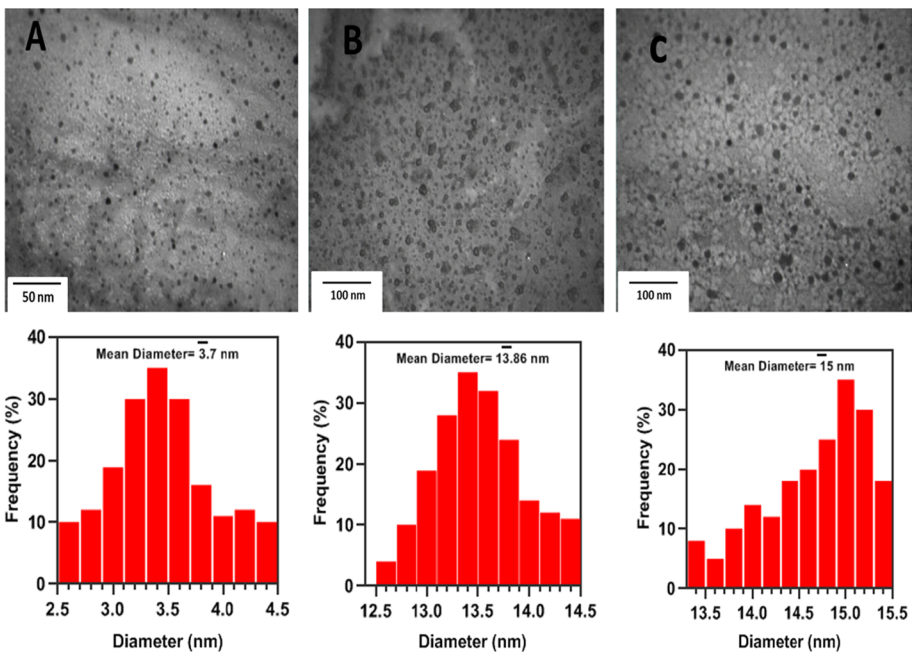

Fig. 2 TEM images and size distibution histogrsms of US-Fe (A), Fe-Gd (B) and Fe_3O_4–Au/Gd (C)

about 5 nm and the size of RGD@Fe_3O_4-Au/Gd NPs was about 15 nm (Fig. 2A–C), this size of NPs was desirable to achieve the purpose of our study. The morphology of NPs, as shown in TEM images (Fig. 2A–C), was spherical. Figure 3A shows the Zeta potential

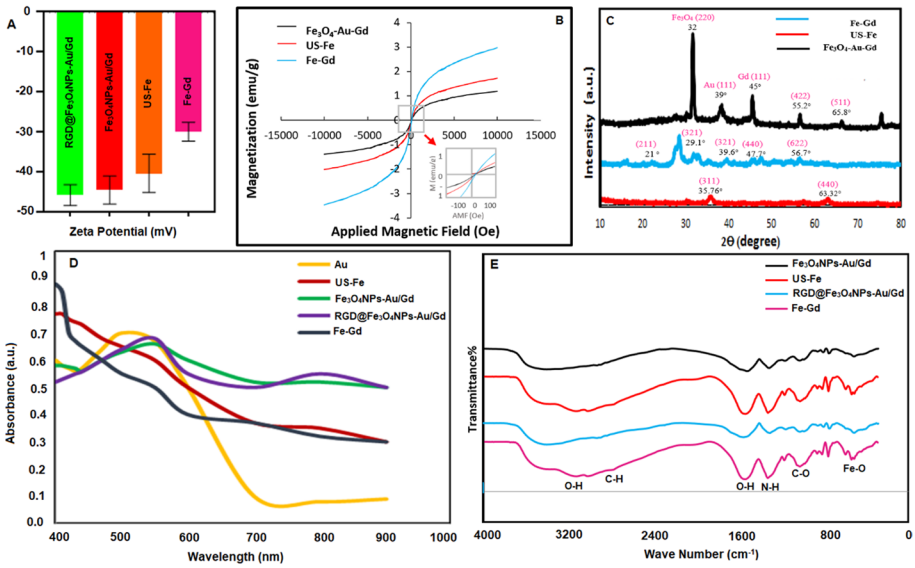

Fig. 3 **A** Zeta potential of US-Fe, Fe-Gd, Fe_3O_4-Au/Gd and RGD@Fe_3O_4-Au/Gd; **B** VSM of US-Fe, Fe-Gd and Fe_3O_4-Au/Gd; **C** XRD patterns of US-Fe, Fe-Gd, and Fe_3O_4-Au/Gd; **D** UV–visible spectrea of US-Fe, Au, Fe-Gd, Fe_3O_4-Au/Gd and RGD@Fe_3O_4-Au/Gd; **E** FTIR of US-Fe, Fe-Gd, Fe_3O_4-Au/Gd and RGD@Fe_3O_4-Au/Gd

Table 1 Characterization of synthesized NPs

Sample	TEM diameter (nm)	DLS (nm)	Zeta (mv)
US-Fe	3.78	11.8	− 30
Fe-Gd	13.86	43.56	− 41
Fe_3O_4-Au/Gd	15	115.2	− 44.4
RGD@Fe_3O_4-Au/Gd	NA	124.4	− 45.7

Table 2 The hysteresis loops of US-Fe, Fe-Gd and Fe_3O_4-Au/Gd (applied magnetic field ranges from -15,000 to 15,000)

Number	Sample	Magnetization (emu/g)
1	US-Fe	1.8
2	Fe-Gd	3
3	Fe_3O_4-Au/Gd	1.1

of US-Fe, Fe-Gd, Fe_3O_4-Au/Gd, and RGD@Fe_3O_4-Au/Gd; also their values are listed in Table 1. Figure 3B shows the lobes' hysteresis of US-Fe, Fe-Gd and Fe_3O_4-Au/Gd measured by VSM. According to Fig. 3B, NPs, especially Fe_3O_4-Au-Gd NPs, have strong paramagnetic properties. As shown in Fig. 2B, nanoparticle Fe-Gd has a magnetization of 3.21, nanoparticle US-Fe has a magnetization of 1.87, and nanoparticle Fe_3O_4-Au/Gd has a magnetization of 1.31, that simultaneous coating of nanoparticles with gold and gadolinium decreased the magnetization of nanoparticles (Table 2). Abdul Mohsen et al. reported that $Ni_{0.1}Ba_{0.9}Fe_2O_4$ magnetic nanoparticles prepared by NaOH was more super paramagnetic compared to samples synthesized with NH_4OH, depending on the particle size and aspect ratio, showed higher magnetic saturation and lower coercivity

(Abdel-Mohsen et al. 2022). Figure 3C shows the X-ray diffraction patterns of US-IO, Fe-Gd, and Fe_3O_4-Au/Gd NPs. According to Fig. 3C, as the size of the NPs increases, the width of the reflection curves increases, which corresponds to Scherer's formula. The intensity of the scattered radiation depends on the material, number, and distribution of atoms in the sample plates. There were peaks at angles of 32, 39, and 45 that indicated the presence of iron oxide, gold, and gadolinium, respectively. After the formation of the nanocomplex, the peak of Fe_3O_4 in RGD@Fe_3O_4-Au/Gd was the same as the XRD of Fe_3O_4. The data confirm the successful synthesis of the Fe_3O_4-Gd-Au nanocomplex without changing the magnetic phase. Peak intensities increase when they are in higher concentrations (Zhu-Liang et al. 2016).

On the other hand, based on the results of UV–visible spectra, RGD@Fe_3O_4-Au/Gd and Fe_3O_4-Au/Gd exhibited maximal absorption in the range of 550 nm (Qiu et al. 2009). This data indicated the presence of small gold particles on the iron oxide core, while US-Fe and Fe-Gd had no absorption peak in this area (Fig. 3D). Once the Fe_3O_4 magnetic NPs were coated with Au dots, an absorption peak at 550 nm was observed, all the same. The formation of RGD@Fe_3O_4-Au/Gd NPs was also confirmed by FTIR measurements. As shown in Fig. 3E, the peaks of 3367, 2926, and 1557 cm^{-1} correspond to the O–H bond of dextran and water, the CH_2 bond of dextran and the carbonyl bond of aldehyde dextran group, respectively. The peaks of 3310, 2962, and 1557 cm^{-1} belong to the O–H bond of carboxymethyl dextran and water, asymmetric carboxyl group carbonyl, and symmetric carboxyl group carbonyl, respectively (Xu et al. 2016). The peak at 557 cm^{-1} corresponds to the Fe–O bond. The peak of the carbonyl citrate group appeared above 1700 cm^{-1}, while the peak of the carbonyl citrate group attached to the surface of the magnetite NPs appeared at 1611 cm^{-1}. The shift is due to the complexation with the magnetite NPs. These results were consistent with the findings of Nigam et al. (Nigam et al. 2011). The peak at 1540 cm^{-1} corresponds to the strong primary bond of an amine (N–H). The amide bond was created by the bond between amines and carboxyl groups, that peaked at 1606 cm^{-1}, which has also been reported by Zhang et al. (Zhang et al. 2014). The peak at 1630 cm^{-1} is associated with the presence of amide bonds. The peak at 550 cm^{-1} corresponds to the Fe–O bond of iron oxide NPs. There was an overlap between the binding of the peptide to the previous amide groups and appeared at 1630 cm^{-1}. Similar results have been reported by Bandekar (Bandekar 1992).

Relaxation rates and MRI performances of RGD@Fe_3O_4-Au/Gd

There were three different complexes with different ratios of iron and gadolinium (with the molar ratio of gadolinium to iron being equal to 0.5, 1, and 2). Due to the close responses of different concentrations of NPs and considering the toxicity of gadolinium, the complex with a ratio of 0.5 was selected as the optimal concentration (Fig. 4). The findings regarding the parameters r_1, r_2, and r_2/r_1 are reported in Table 3. USPIO NPs have low values of r_1, which can be enhanced once the NPs are combined with gadolinium oxide or gadolinium particles. Gd^{3+} is the most well-known T1-weighted contrast agent for clinical use. However, the main challenge in the clinical application of gadolinium is its toxicity. Therefore, significant efforts have been made to reduce the toxicity of gadolinium based on nanomaterial platforms (Ramalho et al. 2016). Based on the results

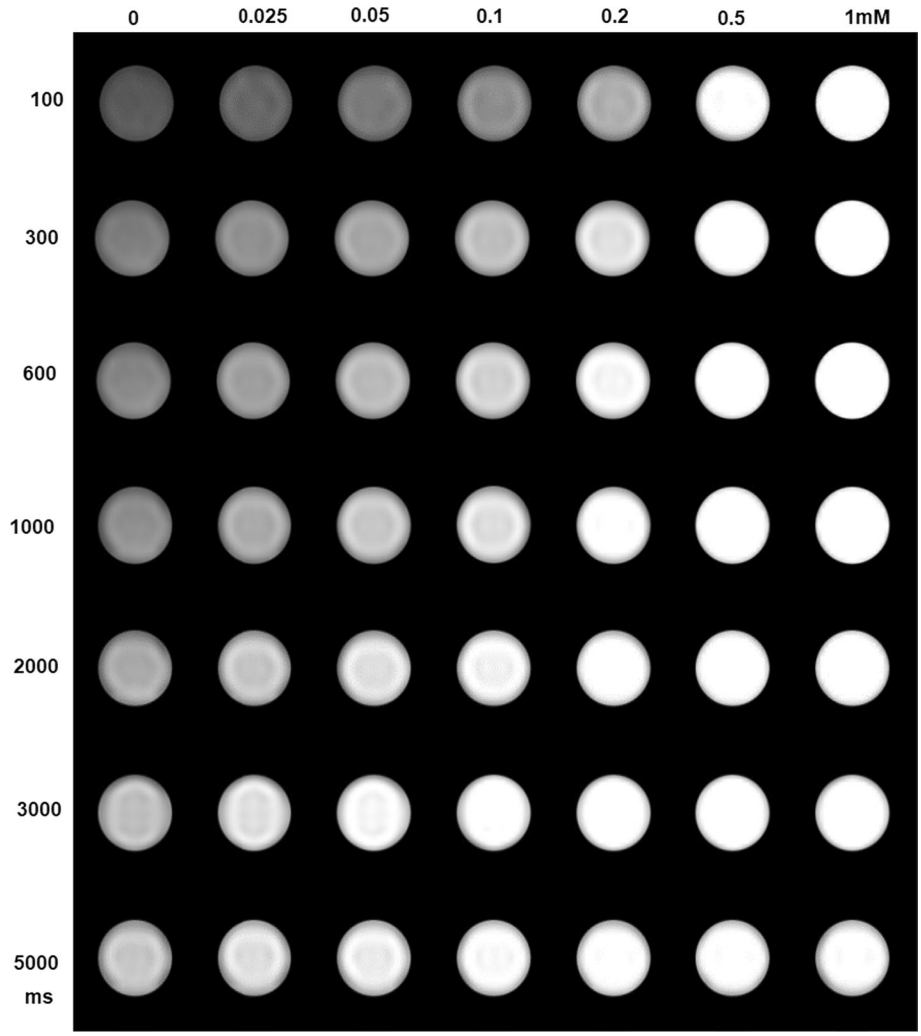

Fig. 4 MRI images relaxation of Fe_3O_4.Au/Gd@RGD in different TRs (from 100 to 5000) and concentrations of 0.025, 0.05, 0.1, 0.2, 0.5, and 1 mM and water as a control group

Table 3 Relaxometry of clinical Dotarem, US-Fe, Fe-Gd and Fe_3O_4-Au/Gd in Tesla field 3

Number	Sample	r_1 [mM^{-1} s^{-1}] (Fe)	r2 [mM^{-1} s^{-1}] (Fe)	r_2/r_1
1	DOTAREM	3.129	3.98	1.29
2	US-Fe	0.265	0.737	2.781
3	Gd/Fe = 1/2	42.63	59.93	1.405
4	Fe_3O_4-Au/Gd	23.5	36.8	1.56

obtained in the present study, r_1 of iron oxide NPs was increased (0.265 vs 23.5) by adding gadolinium to the complex. The large number of Fe^{3+} and Gd^{3+} ions with unpaired electrons on the surface of the NPs causes high r_1 relaxivities. Iron NPs show lower T2 relaxation compared to larger ones because of low magnetic torque. The r_2/r_1 ratio is an important factor for estimating the performance of T1 contrast agents. The r_2/r_1 ratios of US-Fe, Fe-Gd and Fe_3O_4-Au/Gd were 2.781, 1.405, and 1.56, respectively (Table 3).

According to previous studies, if the rate of r_2/r_1 of the contrast agent is less than 5, it is then categorized as a T1-weighted contrast agent. This ratio, however, has recently been reduced to 2 (Demirer et al. 2015). This indicates that our nanocomplex can technically be regarded as a positive contrast agent. MR images of Fe_3O_4-Gd/Au at different concentrations are shown in Fig. 3, based on which tubes containing higher concentrations of Fe_3O_4-Gd/Au appear brighter in T1-weighted images. With the addition of gold to the nanocomposite, the relaxation rates, r_1 and r_2, decreased. Decreased comfort might have been due to reduced magnetic saturation, loss of interaction, and reduced exchange interaction with water nuclei. Our results concerning the addition of gold to iron oxide and the reduction of r_1 and r_2 are consistent with the findings of Brennan et al. (2020). They found that the larger the size of the gold NPs, the greater the reduction in the above-mentioned parameters (Brennan et al. 2020). Ultimately, we managed to develop a nanocomplex with a higher r_1 and r_2/r_1 ratio close and comparable to commercially available contrast agents, including gadolinium-based contrast agents (Table 3).

In vitro experiments

MTT assay

Four cell lines (MDA-MB-231, MCF-7, MCF-10a and SKBR-3) were treated with different concentrations of NPs for 24 h, the biocompatibility of the latter was then assessed by MTT assay. The results showed that at concentrations below 2 mM cell survival was significantly diminished (Fig. 5).

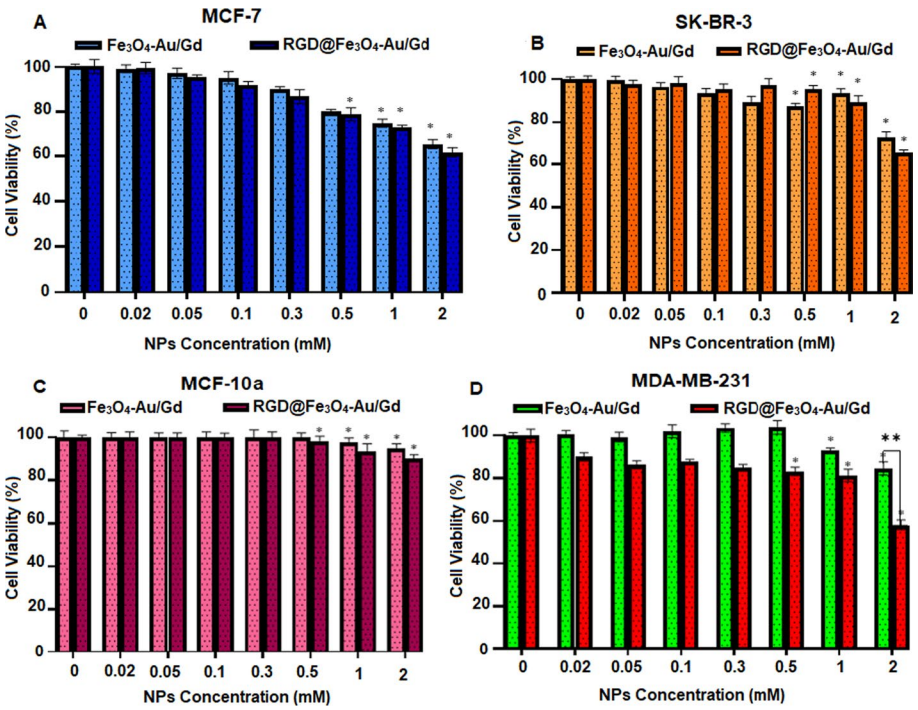

Fig. 5 MTT assay results of MCF-7. **A** SK-BR-3, **B** MCF-10a, **C** and MDA-MB-231. **D** Cell lines which were treated with Fe_3O_4Au/Gd@RGD and Fe_3O_4AuGd at a different concentration (0–2 Mm). (*significant difference with the control group, **significant difference of NPs with and without peptide at a specific concentration P-value < 0.05)

Toxicity was higher in cell groups treated with peptide-bound NPs than in groups treated with peptide-free NPs. This is due to the internalization of NPs by binding to the $\alpha_v\beta_3$ integrin receptor. Only in the MDA-MB-231 cell line and at a concentration of 2 mM there was a significant difference between the groups treated with RGD@Fe_3O_4-Gd/Au and Fe_3O_4-Gd/Au NPs. This is due to the high expression of the αvβ3 receptor on the MDA-MB-231 cell line compared to the three cell lines MCF-7, MCF-10a, and SKBR-3 cell (Liu et al. 2008). The toxicity of NPs was very low in the MCF-10a cell line as a control group. NPs toxicity increases in tumor cells because of the insufficient specificity of the tumor cells (Neshastehriz et al. 2018). According to the obtained data and previous articles, the concentration of 0.05 mM was chosen as the appropriate concentration for the upcoming experiments.

MR imaging incubation time

The incubation times of the NPs were 3, 6, 12 and 24 h for MR imaging. The signal intensity was measured in similar groups with different incubation times, but since there was no significant difference between among different incubation times ($P > 0.05$), the study was proceeded with 24-h incubation.

In vitro MR imaging

T1-weighted MR images were taken from MDA-MB-231, MCF-7, MCF-10a and SKBR-3 cells treated with RGD@Fe_3O_4-Gd/Au and Fe_3O_4-Gd/Au. Different cell lines were examined to obtain the SNR in the T1-weighted MRI (TE = 12 ms, TR = 600 ms). By calculating SNR and ΔSNR, the uptake of NPs was measured in different cell lines (Fig. 6). In this study, SNR and ΔSNR were obtained with the formulas mentioned in the previous section.

Four groups of healthy cell line MCF-10a, positive integrin MDA-MB-231, $\alpha_v\beta_3$ mean expression and negative integrin MCF-7 were located in this study. The uptake of NPs was investigated in different cell groups (0, 100,000, 500,000, 2,500,000 and 5,000,000 cells) for each cell line by calculating ΔSNR. The values of ΔSNR in MDA-MB-231, SK-BR-3, MCF-7, and MCF-10a cell lines treated with RGD@Fe_3O_4-Gd/Au NPs were 163.8 ± 1.1, 111 ± 2.2, 61.21 ± 1.1, and 32.05 ± 1.3, respectively. Also, these values in MDA-MB-231, SK-BR-3, MCF-7, and MCF-10a cell lines treated with Fe_3O_4-Gd/Au NPs were equal to 138.59 ± 1.3, 93.486 ± 1.1, 52.4 ± 1.2, and 27.24 ± 2.2, respectively (Fig. 6).

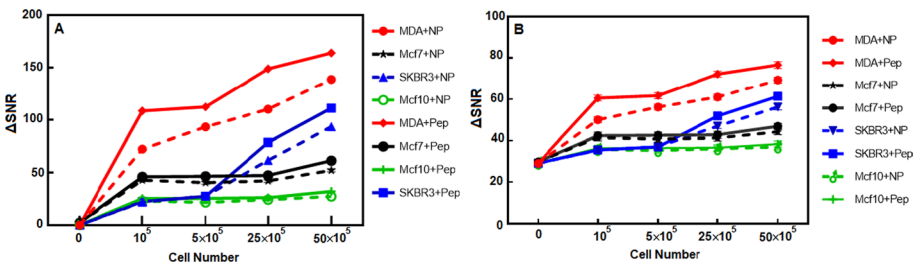

Fig. 6 SNR (A) and ΔSNR (B) in MRI images with weight T1 with TE = 12 and TR = 600 ms and different cell groups (from 0 to 550,000 cells) of MCF-7, MCF-10a, SK-BR-3 and MDA-MB-231 cell lines, which were treated with Fe_3O_4-Au/Gd@RGD and Fe3O4-Au/Gd at a concentration of 0.5 mM and incubation time of 24 h

Finally, T1-weighted MR imaging showed that the present nanocomplex performed better than commercially available contrast materials (Dotarem) in terms of signal enhancement. During the "improved retention and permeability" phenomenon, NPs might accidentally leak through the blood vessels that feed the tumors. The expected therapeutic results cannot be fully achieved using the passive method because NPs may be eliminated by the reticuloendothelial system. There have been a great many attempts to exploit targeted delivery systems, in which NPs are augmented with certain antibodies or peptides to target their corresponding receptors on cancer cells. The high specificity and dependence of peptides make them suitable for the active targeting of tumors. Integrins are the main target of the peptide-coated NPs. Integrins are cell-surface proteins that bind cells to the extracellular matrix and provide a signal pathway for communication between the cell and the matrix. $\alpha_v\beta_3$ integrin is the most used targeting peptide for diagnostic and therapeutic purposes. The $\alpha_v\beta_3$ integrin receptor is expressed on the surface of cancer cells and angiogenic endothelial cells (Liu et al. 2008). This receptor can be identified by the presence of an RGD peptide. The results of the present study showed that the MDA-MB-231 cell line had the highest difference between the uptake of peptides-bound and peptide-free NPs, while the reference MCF-10a cell line exhibited the least difference. Our study indicated that the expression of α5- and αv-integrin heterodimers was increased in invasive breast cancer cell lines (MDA-MB-231) compared to less-invasive breast cancer cell lines such as SK-BR-3. In invasive breast cancer cell lines with high $\alpha_v\beta_3$ receptor expression, NPs often enter the cell through active targeting. The expression of this receptor was very low in MCF-7 and MCF-10a cell lines because the differences in SNR were not significant in the group treated with targeted and non-targeted NPs ($P \leq 0.05$). The results of this study regarding active targeting of RGD peptides in cancer cell lines were consistent with previous studies (Wu et al. 2017). Finally, T1-weighted MR imaging of breast cancer cells confirmed that our nanocomplex did perform better than the already existing commercial contrast materials (Dotarem) in terms signal enhancement.

Determination of radiotherapy efficiency on MDA-MB-231 cells by MTT method

In this study, we designed and synthesized the RGD@Fe_3O_4-Au/Gd nanocomplex and investigated its properties as a radiosensitizer in treatment of breast cancer cell lines. To assess the radiosensitizing effect of NPs, MDA-MB-231 cells were incubated with NP concentrations of 0.02–1 mM/mL for 24 h, and then exposed to 2 Gy of 6 MV X-ray radiation. Toxicity results were obtained for four treatment groups including control group, NPs group, radiotherapy group, as well as radiotherapy and NPs (Fig. 7).

The survival rates in the groups receiving RGD@Fe_3O_4-Au/Gd and Fe_3O_4-Au/Gd and simultaneous radiations were 46.49% and 55.21%, respectively, while the survival rate in the individual radiation group was 87.9% (in concentration of 0.5 mL) (Fig. 7). According to the results, the combination therapy group of NPs and radiotherapy had significantly lower survival rates, indicating high radiosensitivity of RGD@Fe_3O_4-Au/Gd, as well as a synergistic effect) 46.49% cell viability (in combination therapy. The DEF for targeted and non-targeted NPs according to the formula in "Determination of SNR and ΔSNR parameters" section was 1.89 and 1.59, respectively. The increase in dose factor might have been due to the presence of gold and iron NPs. It can be stated that the difference

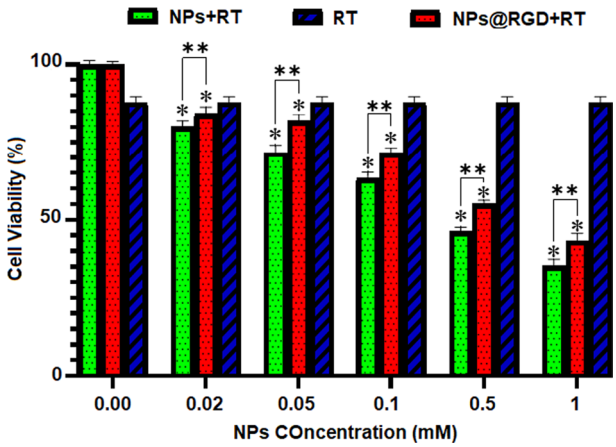

Fig. 7 Changes in the survival rate of MDA-MB-231 cells in X-ray treatment of 6 MeV at the dose of 2 Gy and a dose of 200 C/min in the presence Fe_3O_4-Au/Gd@RGD, Fe_3O_4-Au/Gd and absence of NPs (*significant difference with the control group, **significant difference of NPs with and without peptide at a specific concentration P-value < 0.05)

DEF between RGD@Fe_3O_4-Au/Gd and Fe_3O_4-Au/Gd could be due to the specific function of RGD@Fe_3O_4-Au/Gd on MDA-MB-231 cells. So far, the mechanism of action of SPIONs as radiosensitizers in cancer therapy remains unexplored. Stefanie et al. investigated the formation of ROS in SPION-loaded MCF-7 cells which had been exposed to X-rays. They showed that citrate-coated SPIONs NPs in the presence of X-rays could increase ROS generation by up to 240% (Klein et al. 2012). Gd-based NPs can be used for enhancing radiation dose by inducing activation of the autophagy pathway, which improves the effectiveness of radiotherapy, while reducing collateral damage (Li et al. 2021). Many studies have shown that radiosensitization with ultra-small gadolinium-based NPs leads to complex damage in vitro (Lux et al. 2015). Dose factor analysis showed that gold-coated iron oxide NPs have the potential to be used as radiosensitizers. Gold NPs have been considered as radiosensitizers due to their high biocompatibility, easy synthesis, functionalization, high density and atomic number (Neshastehriz et al. 2018). Wang et al. investigated thioglucose-AuNP as a radiosensitizer in the breast cancer cell line MDA-MB-231. Their results showed that the NPs could reduce cell survival by increasing the sensitivity of cells to radiation (Wang et al. 2015). Our nanocomplex, which was a combination of iron oxide, gold and gadolinium NPs, was also able to act as a radiosensitizer and confirmed the findings of previous studies.

Flow cytometry results

Apoptosis and necrosis are two of the most common ways of stress-induced cell death that may occur in response to X-rays. In the majority of cell deaths, the environment causes inflammation and damage to nearby cells. Apoptosis is an actively planned death that does not cause inflammation and damage to neighboring cells. The inflammatory response of tissues and cells in necrosis leads to reduced efficiency and disruption of treatment. An effective treatment is one which is able to induce apoptosis as the main pathway in cell death. Therefore, in this study, Annexin-V FITC/PI staining kit was used to evaluate the induction of cell death by therapeutic methods applied to evaluate the

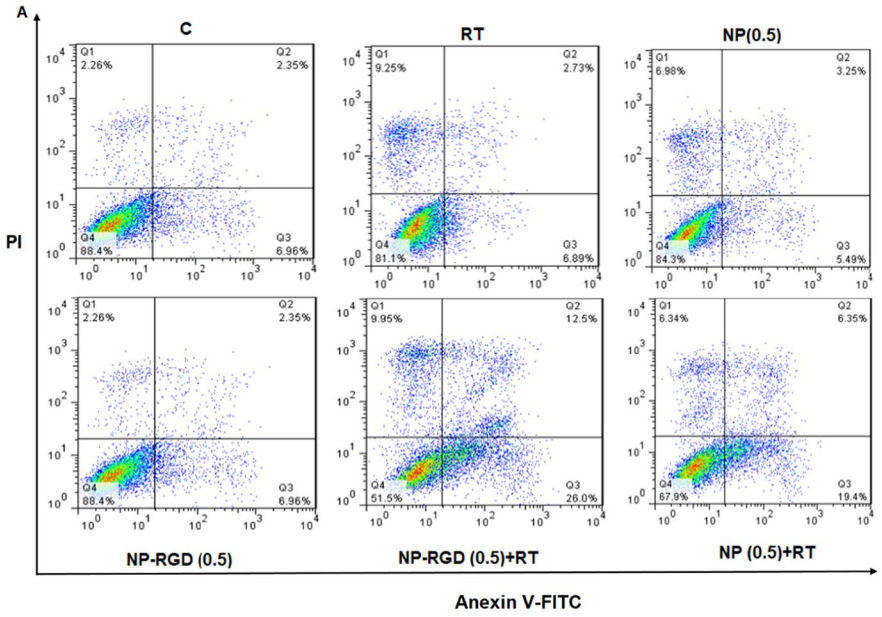

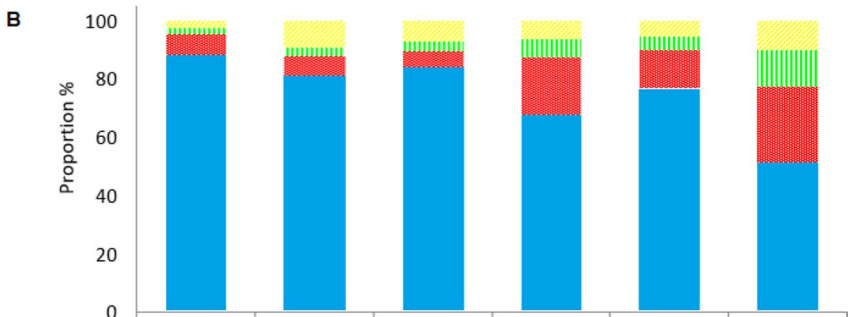

	Ctrl	RT	NP 0.5	NP 0.5+RT	NP RGD 0.5	NP RGD 0.5+RT
Necrosis (%)	2/26	9/25	6/98	6/34	5/39	9/95
Late Apoptosis (%)	2/35	2/73	3/25	6/35	4/52	12/5
Early Apoptosis (%)	6/96	6/89	5/49	19/4	12/9	26
Live Cells (%)	88/4	81/1	84/3	67/9	77/2	51/5

Fig. 8 **A** Apoptosis analysis to determine death modes of MDA-MB-231 cells after receiving radiotherapy, Fe_3O_4-Au/Gd and Fe_3O_4-Au/Gd@RGD NPs alone and combination. **B** Proportion of apoptotic cell death for MDA-MB-231 cells. Abbreviations: C (control), RT (radiotherapy at the dose of 2 Gy), NP 0.5 (Fe_3O_4-Au/Gd at concentration of 0.5 mM), NP-RGD 0.5 (Fe_3O_4-Au/Gd@RGD at concentration of 0.5 mM)

effect of apoptosis on cells. The results were reported as a curve with FLI axes (Fig. 8). Experiments related to the rate of apoptosis were performed on MDA-MB-231 cells. It was already reported that the $\alpha_v\beta_3$ receptor is overexpressed on the surface of MDA-MB-231 cancer cell line, rendering it a good choice for comparison between targeted and non-targeted NPs (Pecheur et al. 2002). The rate of apoptosis was increased by 12.5% following treatment with RGD@Fe_3O_4-Au/Gd and radiation (RT). However, treatment with Fe_3O_4-Au/Gd and RT only increased apoptosis by 4.52%. The rate of apoptosis in NPs with RGD@Fe_3O_4-Au/Gd and Fe_3O_4-Au/Gd and RT alone was 4.52, 3.25, and 2.73%, respectively (Fig. 8). The results show that the apoptotic pathway of cell death is more dominant than necrosis. This is a hallmark of effective treatment because

apoptotic death is an actively planned death that prevents the release of intracellular material and inflammation and damage to neighboring cells, while necrotic death is an inactive and accidental death due to environmental disturbances that cause inflammation and damage to neighboring cells. The type and structure of NPs, concentration, cell type, and incubation time are major factors affecting the process of apoptosis. Therefore, NP-based radiotherapy, in addition to significantly increasing the mortality of MDA-MB-231 cells, which is a photon-sensitizing property of NPs, also directs the path of cell death to apoptotic death. The rates of apoptosis and necrosis were shown to be 54.9% and 54.9%, respectively, by Mir Rahim et al., who measured the effect of RT on a KB cell line upon being treated with Fe_2O_3 NPs (Mirrahimi et al. 2019). The effect of 6 MV radiation on a KB cell line in the presence of Fe_3O_4 was measured by Safari et al. Their results showed that combination therapy could cause apoptosis and necrosis 1.02 and 33 times, respectively (Safari et al. 2020). The data from our study were found to be consistent with those of the previous studies (Almalik et al. 2017; Diagaradjane et al. 2008; Neshastehriz et al. 2017).

ROS test

To increase the efficacy of radiation, iron oxide and gold NPs can be utilized to produce ROS. Designing a treatment that can promote ROS production in a controlled manner would be invaluable to cancer treatment programs (Song et al. 2019). Due to fast cell proliferation and metabolism, cancer cells are more susceptible to oxidation than normal cells, so the excess ROS stress can affect the relatively low oxidant capacity and disrupt the redox homeostasis inside cancer cells, leading to toxicity. When iron oxide NPs are internalized by cells, they proceed to stimulate the generation of ROS via one of two pathways. The release of ion in the cytosol leads to the participation of iron ion in the Haber–Weiss cycle or the surface of iron oxide NP, which can be a catalyst for the Haber–Weiss cycle (Hauser et al. 2016). Misawa et al. found that gold NPs with smaller diameters and larger surfaces lead to higher ROS production. This is probably due to the effects of catalysts (Almalik et al. 2017). Other authors have reported higher levels of ROS for smaller gold NPs (Neshastehriz et al. 2017). In addition to size, ROS may also depend on the performance or surface coverage of NPs, as evidence from a report suggests that hydrophobic coatings such as dextran, have higher levels of ROS (Diagaradjane et al. 2008). Our therapeutic results showed that MDA-MB-231 cells treated with RGD@Fe_3O_4-Au/Gd and X-ray had the highest production of reactive oxygen species and resulted in the death of MDA-MB-231 cell line (Fig. 9).

Conclusions

In summary, we synthesized RGD@Fe_3O_4-Au/Gd NPs as a targeted theranostic nanocomplex for enhanced T1-weighted MR imaging and radiosensitization of cancer cells overexpressing $\alpha_v\beta_3$ receptors. The synthetized RGD@Fe_3O_4-Au/Gd NPs possessed good colloidal stability and biocompatibility, 2.8-fold improved ΔSNR in comparison with Fe_3O_4-Au/Gd (163.8 ± 1.1 vs 59 ± 1.3), and specific targeting of MDA-MB-231 breast cancer cells expressing $\alpha_v\beta_3$ receptors. In experiments regarding the rate of apoptosis in MDA-MB-231 cells, RGD@Fe_3O_4-Au/Gd and RT increased the rate of apoptosis in comparison with Fe_3O_4-Au/Gd and RT by 2.76-fold (12.5% vs 4.52%). In this study,

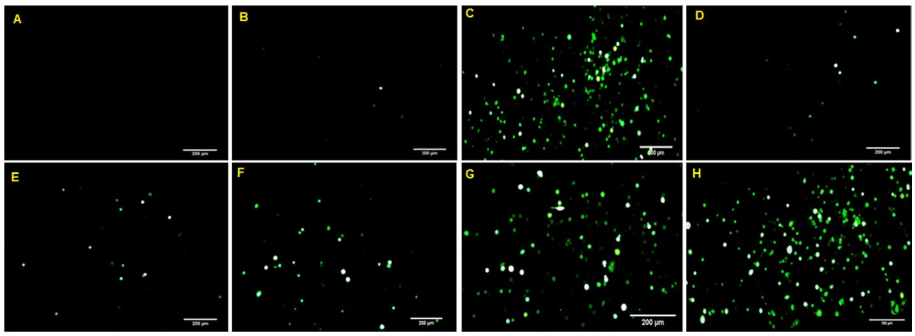

Fig. 9 ROS test results in MDA-MB-231 cells for **A** blank group, **B** negative control group, **C** positive control group, **D** Fe_3O_4-Au/Gd group, **E** RGD@Fe_3O_4-Au/Gd group, **E** radiotherapy group, **G** Fe_3O_4-Au/Gd + radiotherapy group and **H** RGD@Fe_3O_4-Au/Gd + radiotherapy group. The dose of radiotherapy was 2 Gy and the concentration of the NPs was 0.05 mM

we proposed a suitable method for the preparation of a theranostic nanocomplex with higher r_1 and an r2/r1 ratio close and comparable to Dotarem, which increased the contrast of T1-weighted MRI more than the commercially available contrast agent or the reported gadolinium-based contrast agents, all the while being capable of increasing the effect of radiation therapy specifically on breast cancer cells. Therefore, this work constructed a novel theranostic nanocomplex RGD@Fe_3O_4-Au/Gd and provided a useful strategy to enhance their MR imaging effect and therapeutic efficiency.

Methods

Synthesis and characterization of RGD@Fe_3O_4-Au/Gd

Synthesis of carboxylated dextran-coated gadolinium oxide NPs

Dextran (1 g) was dissolved in distilled water (3L) to synthesize gadolinium oxide with a carboxylated dextran coating. Then 3 ml of caustic solution (8 M) was added to the mixture, and the temperature of the mixture was raised to 60–65 °C by immersion in water bath. Afterwards, bromostatic acid (0.4 g) was added and the reaction medium, which became neutralized subsequently. The dextran was then precipitated with ethanol and the resulting NPs were washed three times. Finally, NPs were dried in the oven at 60 °C (Xu et al. 2016). In the next step, Gd $(NO3)_3$ (1 mmol) was added to triethylene glycol (20 ml) in a three-mouth flask and stirred magnetically at 40 °C until the starting material dissolved in the solvent. Simultaneously, NaOH (3 mmol) was added to triethylene glycol (10 ml) and the mixture was placed on a magnetic stirrer at 40 °C. The previous mixture was added to NaOH solution and placed on stirrer at 80 °C for 2 h. Then we add NaOH (0.168 g per 0.5 ml of distilled water) all at once. After, H_2O_2 (3 ml) was added to the reaction solution and sterilized for 2 h. Gd_2O_3 was cloudy due to the formation of ultra-small (US) NPs. To cover the surface, carboxylated dextran (1 mM) was added to the solution at 80 °C and sterilized for 12 h. During this process, unreacted precursors, free ligands, and solvents were removed. The resulting NPs were washed with 40 ml of distilled water three times.

Synthesis of Fe_3O_4 NPs

Fe_3O_4 (US-Fe) was prepared following Massart's co-precipitation method (Massart 1981). First, citric acid (3 mmol) was added to deionized water (50 ml) on a magnetic stirrer. Then $FeCl_3$ (2 mmol) and $FeSO_4.7H_2O$ (1 mmol) were added to the citric acid solution. The products were washed five times in deionized water to remove unreacted ions and remove the colloids from them.

Synthesis of small gold NPs

Aqueous solution (5 ml) of gold salt (10 mM) was mixed with aqueous solution (5 ml) of BSA (50 mg/ml) and mixed at high speed for 2 min. Afterwards, sodium hydroxide solution (1 mM) was added to the mixture and sterilized at 37 °C for 12 h (Zhang 2014).

Synthesis of the final complex

Carboxylated dextran-coated gadolinium oxide and Fe_3O_4 were mixed. The carboxyl groups were activated with the addition of the NHS and EDC. The complex was kept acidic at room temperature for 6 to 7 h. BSA-coated gold NPs were added to mixture. Finally, the synthesized product was washed three times.

Characterization

The morphology and size distribution of the synthesized NPs were determined using a transmission electron microscope (TEM; LEO 906; Zeiss) at an acceleration voltage of 100 kV. The hydrodynamic diameter of NPs and surface charge (zeta potential) were measured by dynamic light scattering (DLS; Malvern Zetasizer Nano ZS-90). The absorption spectra of water-dispersed NPs were recorded using a UV–visible spectrophotometer (UV-2600, Shimadzu, Japan). The synthesized NPs were studied for their surface stabilization and structure via infrared spectrum of absorption (FTIR; AVATAR-370; USA). For this purpose, NPs were kept at 4 °C for 30 days in order to evaluate their stability and resizing. Furthermore, the super paramagnetic property and phases of the synthesized material were investigated via value stream mapping (VSM; LBKFB; Iran) and X-ray diffraction analysis (XRD; Philips pw1730; Netherlands), respectively. ICP-OES (ICP; Perkin-Elmer DV 5300; USA) method was used to determine the concentrations of iron, gadolinium and gold in the nanocomplex.

Cell culture

The in vitro study was conducted on human normal and cancer breast cell lines which were obtained from Pasteur Institute of Iran. MDA-MB-231, MCF-7, SKBR-3 (cancerous) and MCF-10a (reference) cell lines were cultured under controlled conditions (37 °C, humidified environment, and 5% CO_2). The cells were cultured as monolayer in RPMI-1640 and DMEM cell culture media with L-glutamine and $NaHCO_3$, 10% FBS, penicillin (100 U/mL) and streptomycin (100 µg/mL). Cells were harvested after reaching nearly 80% density with trypsin/EDTA 0.25% solution. ICP-OES was used to measure the amount of iron, gadolinium and gold (fg/cell) in the cells.

MTT assay

To assess the cytotoxicity of NPs on cell lines, cells were seeded in 96-well plates with 10^4 cells per well and kept in an incubator over-night. After draining the contents of the wells, 100 mL of culture medium and NPs with different concentrations were added to each well and incubated for 24 h. After the incubation period, the media were removed and 100 µL of MTT solution was added to each sample for 4 h. Then, the surface of the wells was completely emptied, and washed again, after which they were filled with 100 µL of dimethyl sulfoxide (DMSO). The absorption of the optical color was determined by the enzyme-linked immunosorbent assay (ELISA) reader at 570 and 600 nm. Finally, the optimal concentration for diagnosis was determined using the cell survival percentage obtained by MTT assays.

MR imaging

Relaxometry was performed with a 3 Tesla clinical MRI machine (SIEMENS MAGNETOM Prisma). The imaging parameters were selected in a way to achieve the appropriate SNR and resolution. The region of interest (ROI) was defined after the MRI images were obtained. Then, the intensity of the signals obtained from the desired area was obtained for images related to different concentrations in different protocols. In this study, by examining different concentrations, we obtained a relationship to determine the amount of contrast increase in terms of concentration for the designed nanocomplex.

The following steps were taken to determine relaxivity:

- The desired nanocomplex was prepared with certain concentrations of iron within 2-mL microtubes in water.
- The nanocomplex was concentrated by placing microtubes in a water phantom.
- Imaging was performed using the spin-echo protocol.
- 6 TR values (TR = 100, 300, 600, 1200, 1800, 3000 ms) were adopted to determine signal change in a T1 sample with TE = 12 ms.
- A TR of 3000 ms along with 8 echoes (TE = 12, 24, 48, 72, 96, 120, 144, 168 ms) were adopted to calculate signal intensity change in T2 samples.
- At each concentration, signal intensity was visualized using RadiAnt Dicom viewer software.
- Signal intensity graphs were drawn based on different TRs for each concentration using Origin Pro (the 1/T1 value for each concentration was calculated through logarithmically fitting data).
- Signal intensity graphs were drawn in terms of different TEs for each concentration using Origin Pro software. By fitting the data logarithmically, the 1/T2 value was calculated for each concentration.
- Using the values obtained from the above steps, the 1/T1 diagram was drawn according to the concentration using Origin Pro software, and by linear fitting of the obtained values, and we determined the slope of the diagram, which represents the value of r_1.

- Using the values obtained from the above steps, the 1/T2 diagram was drawn according to concentration using Origin Pro software, and by linear fitting of the obtained values, and we determined the slope of the diagram, which represents the r_2 value.

Determination of SNR and ΔSNR parameters

Cellular uptake of nanocomplexes was assessed by in vitro imaging in the water phantom. The cells were cultured in T75 flasks and incubated with RGD@Fe_3O_4-Au/Gd and Fe_3O_4-Au/Gd NPs at a concentration of 0.5 mM for 24 h. The cells were washed with PBS and counted. Five groups with density of 0, 100,000, 500,000, 2,500,000, 5,000,000 number of cells from MCF-7, MCF-10a, SKBR-3 and MDA-MB-231 cell lines were prepared. They were fixed in 2% agar gel and placed in Eppendorf tubes. The control group included cell-free agar gel. SNR and ΔSNR were obtained using Eqs. (1) and (2):

$$SNR = \frac{SI_{mean}}{SD_{noise}}, \tag{1}$$

$$\Delta SNR = \frac{SNR_{post} - SNR_{pre}}{SNR_{pre}} \times 100, \tag{2}$$

where SI mean was the average signal intensity in a sample of the contrast agent. SD noise was the average standard deviation of the field. SNR post was SNR obtained by the contrast agent. SNR pre was SNR obtained in water.

SNR was obtained from T1-weighted MR images and by calculating ΔSNR, the uptakes of NPs by different cell lines were compared.

X-ray irradiation

To investigate the radiosensitivity of NPs, MDA-MB-231 cells treated with NPs were exposed to 2 Gy of X-ray irradiation by Varian linear accelerator (6 MV, 200 cGy/min, Varian Associates Inc., CA, USA). After irradiation, MTT and flow cytometry tests were conducted to evaluate the treatment efficiency. In order to quantify the radiosensitivity of NPs, a dose enhancement factor (DEF) was defined that represented the ratio of the dose deposited in the tumor or cells with NPs, divided by the dose deposited in the tumor or cells without NPs.

Flow cytometry studies

The Annexin V/PI kit was used to evaluate the apoptotic death of MDA-MB-231 cells. First, the culture medium was removed, and the cells were washed with PBS solution (1 ml) and then trypsinized. The cells were centrifuged, the supernatant was removed, and 500 µL of PBS was added to the cells, followed by the addition of 70% cold alcohol (4.5 ml) to the samples, which were carefully pipetted. The stabilized cells were centrifuged for 6 m. The supernatant was drained and dissolved in 5 mL of PBS buffer. The supernatant was drained after the cells were centrifuged again. Finally, 20 µL of Annexin-V was dissolved in buffer (1 ml) and 20 µl of propidium iodide (PI) solution was added to

it, and then 100 µl of the resulting solution was added to the prepared cells. After 15 min of incubation at 15 to 25 °C, the cells were analyzed by flow cytometry.

Reactive oxygen species (ROS)

At first, MDA-MB-231 cells were cultured on 48-well plates. Three control groups were required to perform ROS staining. Cells were treated with H_2O_2 for positive control, and stained cells were used for negative control. The control group that was neither treated nor stained was considered as the blank group. The culture medium was removed after being incubated for 24 h with NPs (0.5 mM). Then, the cells were washed twice with PBS solution. The new medium was added to the cells and then the cells were irradiated with X-ray (2 Gy) by Varian linear accelerators. Following the treatment, DCFH dye was added to the wells after 24 h. Except for the blank group, 150 µL of DCFH dye was added to all the wells and incubated. After an hour, H_2O_2 was added and incubated for 20 min. After washing twice, the 500 µL of medium was added to the wells. Finally, the photograph was taken with a fluorescent microscope.

Statistical analysis

All experiments were performed in triplicate and the data are expressed as mean values ± SD (standard deviation). To evaluate the importance of experimental data using SPSS software (version 16), one-way analysis of variance (ANOVA) followed by Tukey test was used as a post hoc at 95% confidence level. $P < 0.05$ was considered statistically significant.

Abbreviations

MRI	Magnetic resonance imaging
UV–VIS	Visible–ultraviolet spectroscopy
FTIR	Fourier transform infrared spectroscopy
DLS	Dynamic light scattering
TEM	Transmission electron microscope

Acknowledgements
Not applicable.

Author contributions
All authors contributed to the study conception and design. Dr. HG, Dr. HGH and Dr. SRM contributed to material preparation. AA, ZA, Dr. RI, AS, Dr. SS and Prof. SK conducted the experiments and collected the data. The first draft of the manuscript was written by AA and Dr. SS. All the authors reviewed the manuscript. All aspects of the study were supervised by Prof. SK.

Funding
This work was supported by a grant No. 16122 from Iran University of Medical Sciences (IUMS).

Availability of data and materials
The datasets used and/or analyzed during the current study are available from the corresponding author on reasonable request.

Declarations

Ethics approval and consent to participate
This research was approved by Ethics Committee of Iran University of Medical Sciences.

Consent for publication
Not applicable.

Competing interests
The authors have no conflicts of interest.

Received: 16 November 2022 Accepted: 31 May 2023
Published online: 14 June 2023

References

Abdel-Mohsen L, Lafta S, Hashim MS (2022) Comparing the role of NaOH and NH4OH on structural and magnetic properties of spinel Ba ferrite synthesized by autocombustion method. Int J Phys Conf Ser. 1:012081
Almalik A, Alradwan I, Kalam MA, Alshamsan A (2017) Effect of cryoprotection on particle size stability and preservation of chitosan nanoparticles with and without hyaluronate or alginate coating. Saudi Pharm J 25:861–867
Bandekar J (1992) Amide modes and protein conformation. Biochem Biophys Acta 1120:123–143
Brennan G, Bergamino S, Pescio M, Tofail SA, Silien C (2020) The effects of a varied gold shell thickness on iron oxide nanoparticle cores in magnetic manipulation, T1 and T2 MRI contrasting, and magnetic hyperthermia. Nanomaterials 10:2424
Brissette R, Prendergast J, Goldstein NI (2006) Identification of cancer targets and therapeutics using phage display. Current Opinion in Drug Discov Devel 9:363–369
Chang Z-X, Li C-H, Chang Y-C, Huang C-YF, Chan M-H, Hsiao M (2022) Novel monodisperse FePt nanocomposites for T2-weighted magnetic resonance imaging: biomedical theranostics applications. Nanoscale Adv. 4:377–386
Demirer GS, Okur AC, Kizilel S (2015) Synthesis and design of biologically inspired biocompatible iron oxide nanoparticles for biomedical applications. J Mater Chem B 3:7831–7849
Diagaradjane P et al (2008) Modulation of in vivo tumor radiation response via gold nanoshell-mediated vascular-focused hyperthermia: characterizing an integrated antihypoxic and localized vascular disrupting targeting strategy. Nano Lett 8:1492–1500
Fang J, Nakamura H, Maeda H (2011) The EPR effect: unique features of tumor blood vessels for drug delivery, factors involved, and limitations and augmentation of the effect. Adv Drug Delivery Rev. 63:136–151
Fu S, Cai Z, Ai H (2021) Stimulus-responsive nanoparticle magnetic resonance imaging contrast agents: design considerations and applications. Adv Healthc Mater 10:2001091
Gaumet M, Vargas A, Gurny R, Delie F (2008) Nanoparticles for drug delivery: the need for precision in reporting particle size parameters European. J Pharm Biopharm 69:1–9
Ghaghada KB, Ravoori M, Sabapathy D, Bankson J, Kundra V, Annapragada A (2009) New dual mode gadolinium nanoparticle contrast agent for magnetic resonance imaging. PLoS ONE 4:e7628
Hauser AK, Mitov MI, Daley EF, McGarry RC, Anderson KW, Hilt JZ (2016) Targeted iron oxide nanoparticles for the enhancement of radiation therapy. Biomaterials 105:127–135
Hynes RO (2002) Integrins: bidirectional, allosteric signaling machines. Cell 110:673–687
Kamaly N, Xiao Z, Valencia PM, Radovic-Moreno AF, Farokhzad OC (2012) Targeted polymeric therapeutic nanoparticles: design, development and clinical translation. Chem Soc Rev 41:2971–3010
Klein S, Sommer A, Distel LV, Neuhuber W, Kryschi C (2012) Superparamagnetic iron oxide nanoparticles as radiosensitizer via enhanced reactive oxygen species formation. Biochem Biophys Res Commun 425:393–397
Lafta SH (2022) Hydrothermal temperature influence on magnetic and FMR properties of hematite nanoparticles. MAGMA-D-21–02419. https://papers.ssrn.com/sol3/papers.cfm?abstract_id=3989692
Leserman LD, Weinstein JN, Blumenthal R, Terry WD (1980) Receptor-mediated endocytosis of antibody-opsonized liposomes by tumor cells. Proc Natl Acad Sci 77:4089–4093
Li X et al (2019) Light-addressable nanoclusters of ultrasmall iron oxide nanoparticles for enhanced and dynamic magnetic resonance imaging of arthritis advanced. Science 6:1901800
Li H, Zeng Y, Zhang H, Gu Z, Gong Q, Luo K (2021) Functional gadolinium-based nanoscale systems for cancer theranostics. J Control Release 329:482–512
Li H, Wang R, Hong R, Li Y (2022) Preparation, biocompatibility and imaging performance of ultrasmall iron oxide magnetic fluids for T1/T2-weighted MRI. Colloids Surf a: Physicochem Eng Aspects 648:129360
Ling D, Lee N, Hyeon T (2015) Chemical synthesis and assembly of uniformly sized iron oxide nanoparticles for medical applications. Acc Chem Res 48:1276–1285
Liu Z, Wang F, Chen X (2008) Integrin αvβ3-targeted cancer therapy. Drug Dev Res 69:329–339
Lu M, Ozcelik A, Grigsby CL, Zhao Y, Guo F, Leong KW, Huang TJ (2016) Microfluidic hydrodynamic focusing for synthesis of nanomaterials. Nano Today 11:778–792
Lux F, Sancey L, Bianchi A, Crémillieux Y, Roux S, Tillement O (2015) Gadolinium-based nanoparticles for theranostic MRI-radiosensitization. Nanomedicine 10:1801–1815
Lv P-P, Ma Y-F, Yu R, Yue H, Ni D-Z, Wei W, Ma G-H (2012) Targeted delivery of insoluble cargo (paclitaxel) by PEGylated chitosan nanoparticles grafted with Arg-Gly-Asp (RGD). Mol Pharm 9:1736–1747
Massart R (1981) Preparation of aqueous magnetic liquids in alkaline and acidic media. IEEE Trans Magn 17:1247–1248
Mendichovszky IA, Marks SD, Simcock CM, Olsen ØE (2008) Gadolinium and nephrogenic systemic fibrosis: time to tighten practice. Pediatr Radiol 38:489–496
Mirrahimi M et al (2019) Modulation of cancer cells' radiation response in the presence of folate conjugated Au@ Fe2O3 nanocomplex as a targeted radiosensitizer. Clinical Transl Oncol. 21:479–488
Neshastehriz A, Tabei M, Maleki S, Eynali S, Shakeri-Zadeh A (2017) Photothermal therapy using folate conjugated gold nanoparticles enhances the effects of 6 MV X-ray on mouth epidermal carcinoma cells. J Photochem Photobiol b: Biology. 172:52–60
Neshastehriz A, Khosravi Z, Ghaznavi H, Shakeri-Zadeh A (2018) Gold-coated iron oxide nanoparticles trigger apoptosis in the process of thermo-radiotherapy of U87-MG human glioma cells. Radiat Environ Biophys 57:405–418
Nigam S, Barick K, Bahadur D (2011) Development of citrate-stabilized Fe3O4 nanoparticles: conjugation and release of doxorubicin for therapeutic applications. J Magn Magn Mater 323:237–243

Pasqualini R, Koivunen E, Ruoslahti E (1997) αv integrins as receptors for tumor targeting by circulating ligands. Nat Biotechnol 15:542–546
Pecheur I et al (2002) Integrin αvβ3 expression confers on tumor cells a greater propensity to metastasize to bone. FASEB J 16:1266–1268
Qiu J-D, Xiong M, Liang R-P, Peng H-P, Liu F (2009) Synthesis and characterization of ferrocene modified Fe3O4@ Au magnetic nanoparticles and its application. Biosens Bioelectron 24:2649–2653
Rajaee Z, Khoei S, Mahdavian A, Shirvalilou S, Mahdavi SR, Ebrahimi M (2020) Radio-thermo-sensitivity induced by gold magnetic nanoparticles in the monolayer culture of human prostate carcinoma cell line DU145. Anti-Cancer Agents Med Chem 20:315–324
Ramalho J, Semelka R, Ramalho M, Nunes R, AlObaidy M, Castillo M (2016) Gadolinium-based contrast agent accumulation and toxicity: an update. Am J Neuroradiol 37:1192–1198
Safari A et al (2020) Optimal scheduling of the nanoparticle-mediated cancer photo-thermo-radiotherapy. Photodiagn Photodyn Ther 32:102061
Schottelius M, Laufer B, Kessler H, Wester H-Jr, (2009) Ligands for mapping αvβ3-integrin expression in vivo. Acc Chem Res 42:969–980
Shen Z et al (2017) Multifunctional theranostic nanoparticles based on exceedingly small magnetic iron oxide nanoparticles for T 1-weighted magnetic resonance imaging and chemotherapy. ACS Nano 11:10992–11004
Shirvalilou S, Khoei S, Khoee S, Raoufi NJ, Karimi MR, Shakeri-Zadeh A (2018) Development of a magnetic nano-graphene oxide carrier for improved glioma-targeted drug delivery and imaging: in vitro and in vivo evaluations. Chem Biol Interact 295:97–108
Siegel RL, Miller KD, Jemal A (2015) Cancer statistics, 2015. CA: a Cancer J Clin. 65:5–29
Song J et al (2019) Self-assembled responsive bilayered vesicles with adjustable oxidative stress for enhanced cancer imaging and therapy. J Am Chem Soc 141:8158–8170
Wang C, Jiang Y, Li X, Hu L (2015) Thioglucose-bound gold nanoparticles increase the radiosensitivity of a triple-negative breast cancer cell line (MDA-MB-231). Breast Cancer 22:413–420
Wei H et al (2017) Exceedingly small iron oxide nanoparticles as positive MRI contrast agents. Proc Natl Acad Sci 114:2325–2330
Wu P-H et al (2017) Targeting integrins with RGD-conjugated gold nanoparticles in radiotherapy decreases the invasive activity of breast cancer cells. Int J Nanomed 12:5069
Xiao-Dong Z, Chen J, Luo Z, Wu D, Shen X, Song SS, Sun Y-M, Liu P-X, Zhao J, Huo S, Fan S, Fan F, Liang XJ, Xie J (2014) Enhanced tumor accumulation of sub-2 nm gold nanoclusters for cancer radiation therapy. Adv Healthcare Mater 3:133
Xie J et al (2008) Ultrasmall c (RGDyK)-coated Fe3O4 nanoparticles and their specific targeting to integrin αvβ3-rich tumor cells. J Am Chem Soc 130:7542–7543
Xu W, Miao X, Oh IT, Chae KS, Cha H, Chang Y, Lee GH (2016) Dextran-coated ultrasmall Gd2O3 nanoparticles as potential T1 MRI contrast agent. ChemistrySelect 1:6086–6091
Yoo D, Lee J-H, Shin T-H, Cheon J (2011) Theranostic magnetic nanoparticles. Acc Chem Res 44:863–874
Zako T et al (2009) Cyclic RGD peptide-labeled upconversion nanophosphors for tumor cell-targeted imaging. Biochem Biophys Res Commun 381:54–58
Zeng L, Luo L, Pan Y, Luo S, Lu G, Wu A (2015) In vivo targeted magnetic resonance imaging and visualized photodynamic therapy in deep-tissue cancers using folic acid-functionalized superparamagnetic-upconversion nanocomposites. Nanoscale 7:8946–8954
Zhang XD et al (2014) Radiosensitizers: enhanced tumor accumulation of Sub-2 nm gold nanoclusters for cancer radiation therapy (Adv. Healthcare Mater. 1/2014). Adv Healthc Mater. 3:152–152
Zhu-Liang W, Hui M, Fang W, Min L, Li-Guo Z, Xiao-Hong X (2016) Controllable synthesis and magnetic properties of monodisperse Fe $ _ 3 $ O $ _ 4 $ nanoparticles. Chinese Phys Lett. 33:107501–107501

Publisher's Note